Available online at www.sciencedirect.com

jmr&t Journal of Materials Research and Technology

www.jmrt.com.br

Original Article

Microstructural characterization and mechanical behavior during recrystallization annealing of Nb-stabilized type ASTM 430 and Nb-Ti-stabilized ASTM 439 ferritic stainless steels

Leandro Tanure[a,b,*], *Cláudio Moreira de Alcântara*[c], *Dagoberto Brandão Santos*[a], *Tarcísio Reis de Oliveira*[c], *Berenice Mendonça Gonzalez*[a], *Kim Verbeken*[b]

[a] *Department of Metallurgical and Materials Engineering, Universidade Federal de Minas Gerais - UFMG, Escola de Engenharia - Bloco 2, Av. Antônio Carlos, 6627, Pampulha, CEP 31270-901, Belo Horizonte, MG, Brazil*

[b] *Department of Materials, Textiles and Chemical Engineering, Ghent University (UGent), Technologiepark 46, B-9052 Ghent, Belgium*

[c] *Research Department, Aperam South America, Praça 1° de Maio, 09, Centro, CEP 35180-018 Timóteo, MG, Brazil*

ARTICLE INFO

Article history:
Received 28 February 2019
Accepted 10 July 2019
Available online 26 July 2019

Keywords:
Ferritic stainless steel
Texture
EBSD
Mechanical behavior
Drawability
Microstructure

ABSTRACT

A comparison between the niobium-stabilized type ASTM 430, 430Nb, and niobium-titanium-stabilized ASTM 439 ferritic stainless steels with respect to their microstructure and texture at the different stages of recrystallization was performed. The annealed samples were subjected to tensile test and Swift test for evaluation of mechanical behavior and deep drawability, respectively. The heat treatment was carried out on lab-scale cold rolled sheets with 85% thickness reduction as an attempt to mimic the industrial process. Recrystallization occurred first for 430Nb steel with smaller recrystallized grain sizes, less pronounced γ-fiber texture, lower average normal anisotropy coefficient, $\bar{R}$, and limit drawing ratio, LDR. On the other hand, ASTM 439 showed higher yield stress but better drawability. These results are presented and discussed based on microtexture evolution, precipitate characteristics and grain boundary character distributions.

1. Introduction

Ferritic stainless steels (FSS) are, essentially, iron–chromium alloys (chromium content between 11 and 30%) and have been extensively used worldwide because of their good corrosion resistance, good formability, good high-temperature oxidation resistance and lower cost compared to austenitic stainless steels [1,2]. FSS are also well resistant to stress corrosion cracking and localized corrosion, e.g. pitting and crevice corrosion. However, some of the disadvantages of FSS are the susceptibility to intergranular corrosion and the lower plasticity compared to austenitic grades and plain carbon steels [3].

Intergranular corrosion is a consequence of the sensitization phenomenon, where interstitial atoms, such as carbon and nitrogen, precipitate with chromium in the grain boundaries leaving a chromium depleted zone near these precipitates and, therefore, creating areas which are more

* *Corresponding author.*
E-mail: leandro.tanure@ugent.be (L. Tanure).

https://doi.org/10.1016/j.jmrt.2019.07.015

susceptible to corrosion. Besides sensitization, high levels of C and N are responsible for other deleterious effects such as toughness reduction and an increase in ductile-to-brittle transition temperature [3,4].

The control of sensitization can be done in two different ways: reducing carbon and nitrogen contents below a minimum level (e.g. 250 ppm) [5] or adding stabilizing elements (e.g. Ti, Nb, V, Zr) that would form precipitates with carbon and nitrogen rapidly and more stable than the ones possibly formed with chromium. In this way, chromium would remain available in the entire microstructure to form the invisible and adherent chromium oxide layer that gives corrosion resistance to FSS [3,5]. Among the stabilizing elements, Ti and Nb have shown to be the most promising candidates [5,6] and are also able to improve mechanical performance reducing recrystallized grain size [7].

Regarding the lower plasticity, several studies have been carried out to identify parameters that could enhance the formability of stabilized FSS and assist the development of new metallurgical routes [8–13]. It is known that size and distribution of precipitates as well as the amount of stabilizing elements in solid solution affect the final grain size, texture development and, consequently, mechanical properties such as yield stress, elongation and deep drawability [14,15].

Recently [11,12,16], efforts have been made in order to clarify the effect of some parameters (such as heating rate and the initial grain size) on the evolution of microstructure and mechanical behavior during annealing of the Nb-stabilized type ASTM 430, 430Nb alloys as well as on the effect of Nb addition in a Ti-stabilized FSS [13]. The present study, on the other hand, will evaluate and compare the effect of Ti addition on a Nb-stabilized FSS.

In the industry, it is known that the ASTM 439 FSS exhibits better mechanical performance under deep drawing conditions than the Nb-stabilized type ASTM 430 while also showing worse superficial finishing. The purpose of this paper is to assess the microstructure/microtexture and grain boundary character distribution evolution during annealing heat treatment of these two FSS produced in a way that simulates the industrial scale production using electron backscatter diffraction (EBSD) technique as well as characterize the precipitates with the aid of scanning electron microscopy (SEM), energy dispersive X-ray spectroscopy (EDS) and evaluate mechanical behavior of annealed samples by tensile and Swift tests. The main goal of this work is to elucidate how the metallurgical routes and chemical composition affect the microstructural evolution of both steels leading to the abovementioned differences.

2. Experimental work

2.1. Materials

The studied materials were provided by *Aperam South America*. The Nb-stabilized FSS type ASTM 430, 430Nb, whose chemical composition, in weight %, was 0.017C, 0.172Mn, 16.5Cr, 0.022N, 0.233Ni and 0.314Nb while the chemical composition of the Nb-Ti-stabilized FSS ASTM 439 was 0.010C, 0.190Mn, 17.2Cr, 0.011N, 0.20Ni, 0.19Nb and 0.15Ti. Samples from the steel 430Nb were supplied hot rolled and annealed condition whereas the samples from ASTM 439 were supplied hot rolled. Both of them with 4.0 mm thickness. These conditions were identified as "as-received" (AR). The cold rolling was carried out on a laboratory scale aiming 85% thickness reduction until 0.60 mm (samples CR). The annealing was performed with a heating rate of 24 °C/s and soaking time of 24 s for both steels (samples A). The soaking temperatures were 880 °C for 430Nb steel and 925 °C for ASTM 439. Differences in the soaking temperature as well as in the "as-received" conditions followed from the industrial processing route. These are indeed the parameters used on industrial scale, therefore, the experiment was designed to follow and evaluate differences caused by each metallurgical route.

The annealing heat treatment was interrupted at four temperatures to evaluate the samples at different stages of recrystallization, namely: 700 °C (samples T1), 770 °C (samples T2), 800 °C (samples T3) and 830 °C (samples T4).

2.2. Methods

The samples were analyzed via EBSD on the longitudinal sections of specimens that were taken from the central part of the sheets. Besides the standard metallographic preparation procedure (cutting, mounting, grinding and polishing) an additional step of polishing using colloidal silica was required. Samples in the condition "as-received" and "annealed" were scanned through the whole thickness with a step size of 8 μm while the other conditions were scanned with a step size of 0.08 μm in a $50 \times 100\,\mu m^2$ area located at the middle of the thickness. The analyses were performed with the aid of the Scanning Electron Microscope (SEM) FEI-Quanta 200 FEG and the OIM® software. In order to characterize the precipitates, on the annealed samples, images were obtained using the SEM-FEI Inspect 50 equipped with an energy dispersive X-ray spectrometry (EDS) for chemical composition analysis and the samples were etched with Villela.

Tensile tests were performed on the annealed samples, at room temperature, using an INSTRON 5582 equipment. Ultimate tensile strength and yield strength were measured according to the standard ASTM A370-10. The anisotropy of the materials was evaluated through the average normal anisotropy coefficient, $\bar{R}$, and the planar anisotropy coefficient, ΔR, which were calculated using the formulas $(R_0 + 2R_{45} + R_{90})/4$ and $(R_0 - 2R_{45} + R_{90})/2$, respectively, where R_0, R_{45} and R_{90} are the R-value in the directions of 0°, 45° and 90° with respect to the rolling direction. These samples were 15% strained and the test was performed according to the ASTM E517-10 standard. Finally, the Swift test was performed by an Erichsen 14240 equipment to determine the limit drawing ratio, LDR.

3. Results and discussion

3.1. EBSD analysis

3.1.1. As-received condition

Fig. 1 shows the results obtained by EBSD analysis on 430Nb steel "as-received". Fig. 1(a) is a grain orientation spread (GOS)

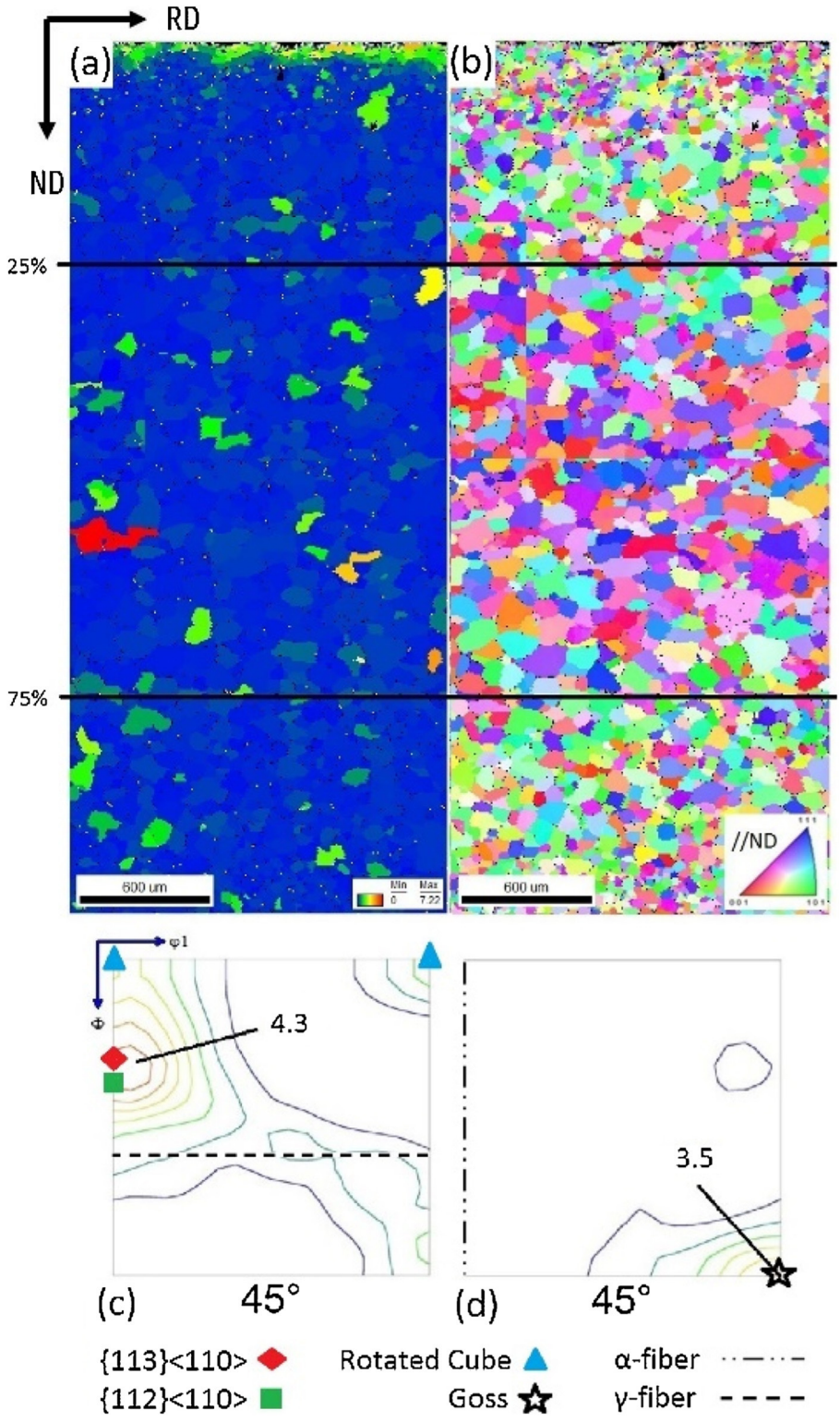

Fig. 1 – 430Nb steel (a) GOS map, (b) IPF map (color code parallel to ND), (c) ODF of the internal (between 25% and 75% lines) region $\varphi_2 = 45°$ and (d) ODF of the external region (above 25% and below 75% lines) $\varphi_2 = 45°$. Texture levels: 1-1.5-2-2.5-3-3.5-4-4.5 times random.

map that represents the orientation spread with respect to an average orientation for each grain, which means that the higher the GOS the higher the average deviation between the orientation of each point in the grain and the average orientation for the grain. Fig. 1(b) is an inverse pole figure (IPF) map showing different crystallographic orientations in a color scale (color code with respect to the normal direction-ND). Fig. 1(c) and (d) show the $\varphi_2 = 45°$ section of the orientation

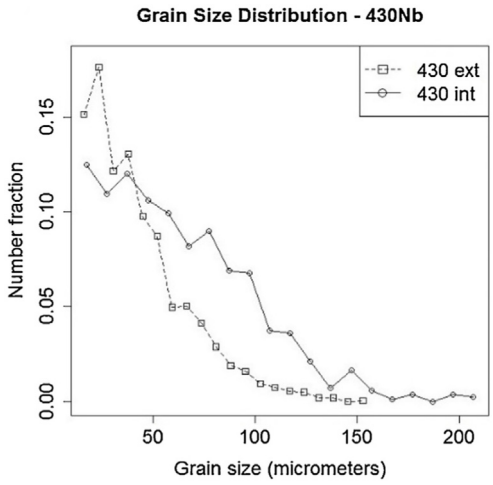

Fig. 2 – Grain Size Distributions of the external (above 25% and below 75% lines) and internal (between 25% and 75% lines) regions of the 430Nb steel.

distribution function (ODF) of the central and external regions, respectively. Fig. 2 represents a graph of the grain size distribution of two distinct regions: external (above the line of 25% of thickness and below the line 75%) and central (between the aforementioned lines). These lines were used to improve the analysis since the regions presented clear differences in grain size and texture.

Fig. 1(a) shows that the GOS ranges from 0 to 7° and, besides a few grains in green at the upper surface, a homogeneous distribution composed mainly by low GOS values (blue grains) in the whole thickness was observed. Larger values of GOS can be related to the presence of dislocation tangles, shear bands, deformation bands and transition bands within the grain. These microstructural features are due to heterogeneities in the plastic deformation and can be associated with the stored energy in the grain [17]. Once the steel 430Nb was annealed after hot rolling, lower values of GOS are expected than those for the ASTM439 steel.

The IPF map in Fig. 1(b) clearly shows differences in the texture and grain size along the thickness. The distributions of the grain sizes are plotted in Fig. 2 where larger fractions of smaller grains are noticed in the external region as a consequence of the strain gradient. The average grain sizes are 62 and 42 μm for the central and external regions, respectively. Recrystallization occurs via nucleation and growth where the grain size is a function of the ratio (nucleation rate)/(growth rate) [18]. When this ratio increases with a decrease in transformation temperature, the final grain size decreases [19] (a larger undercooling provides a higher driving force for nucleation of more grains and reduces the mobility of grain boundaries due to the lower temperature). Therefore ferrite grains decrease in size by accelerated cooling. On the other hand, as the temperature gradient decreases, there is more time for grain growth to occur and fewer nuclei are formed. The effect of annealing heating rate on Nb-stabilized FSS was studied by Rodrigues et al. in more details [11,16].

As can be seen in Fig. 1(c), the central region is dominated by grains belonging to the α-fiber (<110> // Rolling Direction, RD), with a maximum intensity (4.3 times random) on (225) [31 $\bar{3}$6 2], which is close to the components (113) [1$\bar{1}$0] and (112) [1$\bar{1}$0], and minor intensities at the rotated cube, (001) [$\bar{1}\bar{1}$0], Goss, (110)[001], and γ-fiber texture components. The external region, Fig. 1(d), presents, mainly, Goss texture (3.5 times random) which originates from the strong shear deformation. This same profile of texture variation through thickness was also observed by Raabe and Lücke in FSS with 17%Cr after hot rolling [20]. The shear condition is attenuated by the thickness whereas the center is deformed by plain strain allowing the formation of α and γ fibers.

The same analysis as the one performed on 430Nb steel, Figs. 1 and 2, is shown in Figs. 3 and 4 for the ASTM 439 steel.

Fig. 3(a) shows a GOS map ranging from 0 to 13° and displays, consequently, larger GOS values in comparison with 430Nb steel. Small recrystallized grains are concentrated near the surface (blue grains) whereas the recovered grains are located in the internal region (larger GOS values). The IPF map, Fig. 3(b), confirms this observation through the color variation within the grains. It means that there is still stored energy inside these grains from the rolling process. This crystallographic spread, as mentioned before, is due to plastic deformation heterogeneities. Although the hot rolling route of the ASTM 439 steel was capable of producing equiaxed grains, similar features of the deformed state such as slightly elongated grains in the rolling direction and intra grain misorientation, remain present. The annealing performed after hot rolling in the 430Nb steel produced a more recrystallized microstructure when compared to the hot rolling on ASTM 439 if one compares the GOS maps, Figs. 1(a) and 3(a).

Differences in grain size and texture along thickness are also noticed. Thus, the same distribution, in two regions, as applied when analyzing the 430Nb steel, was used. Smaller grains are present in the external region, Fig. 4, with a mean value of 55 μm as well as a high texture intensity on the Goss component, (110)[001], 4.5 times random, Fig. 3(d). Similar behavior was observed in the as-received 430Nb.

For the internal region, besides the larger grains (mean value of 76 μm) texture maxima along the α-fiber, γ-fiber and on the rotated cube were found. A peak is present (3.4 times random) close to (334) [4$\bar{8}$3] component. As the rolling route of this material was able to promote dynamic recovery and no annealing was performed afterwards, some differences are expected in comparison with steel 430Nb, such as a less recrystallized microstructure. Due to the high stacking fault energy (SFE), FSS are prone to fast dynamic recovery during hot rolling which reduces the probability of nucleation of new grains with random orientation [21].

3.1.2. *Cold rolled condition*

Fig. 5(a) and (b) show IPF maps of the 430Nb and ASTM 439 samples, respectively, in the cold rolled condition as well as the corresponding ODF sections, Fig. 5(c) and (d).

As can be seen in Fig. 5(a) and (b), the IPF maps display a severely deformed microstructure for both steels. The predominance of specific colors (pink and orange in 430Nb and blue and purple in ASTM 439) is an indication of a strong texture. According to the ODF, steel 430Nb presented α-fiber texture components peak at (113) [1$\bar{1}$0], 20 times random, and

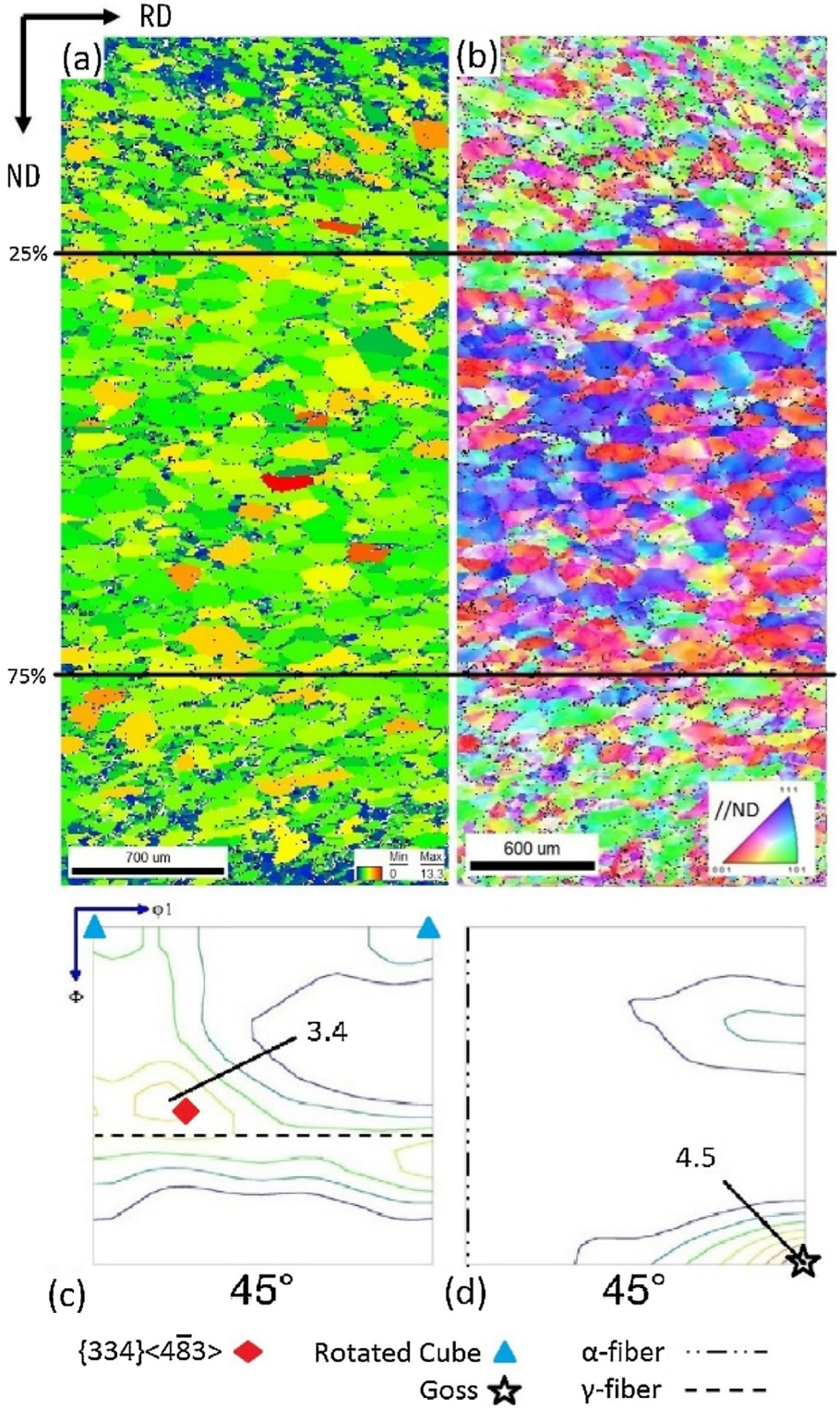

Fig. 3 – ASTM 439 steel (a) GOS map, (b) IPF map (color code parallel to ND), (c) ODF of the internal region $\varphi_2 = 45°$ and (d) ODF of the external region $\varphi_2 = 45°$. Texture levels: 1-1.5-2-2.5-3-3.5-4-4.5.

rotated cube, while ASTM 439 showed main intensity along the γ-fiber and α-fiber, maximum of 12.7 times random at (447) [1$\bar{1}$0]. These results are consistent with previous observations of Raabe and Lücke for the texture of heavily cold rolled ferritic stainless steels [20].

Comparing the texture of the internal region from the "as-received" materials with "cold rolled" conditions, both steels presented strengthening of the previous dominant texture, namely the α-fiber in 430Nb and both α and γ-fiber in ASTM 439.

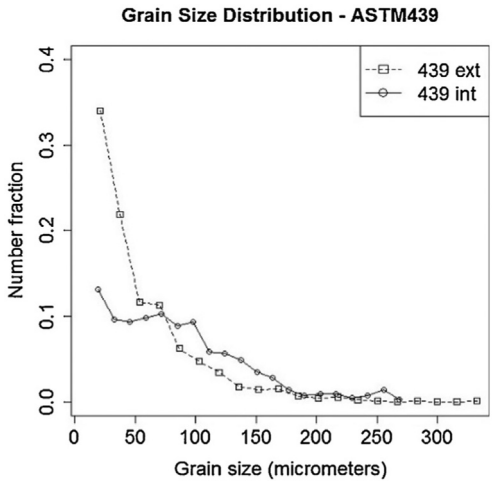

Fig. 4 – Grain Size Distributions of the external (above 25% and below 75% lines) and internal (between 25% and 75% lines) regions of the ASTM 439 steel.

Deformation in metals and alloys with cubic structure is accommodated by slip and/or twinning. The predominant mechanism is largely determined by stacking-fault energy, temperature and strain ratio. Generally, metals with moderate and high stacking-fault energy (body centered cubic, bcc, structure) will deform by slip [17]. During plastic deformation in polycrystalline metals, several grains are subjected to the same external stresses, but only the ones most favorably orientated, i.e. with a larger Schmid factor, will have their slip systems activated. However, the neighboring grains (with lower Schmid factor values) will impose restrictions to the deformation compatibility inducing their rotation and also generating dislocations where orientation differences are more pronounced. These grain rotations are the main cause of the above mentioned deformation heterogeneities, generating deformation gradients and, therefore, stored energy gradients within and between grains affecting the recovery and recrystallization phenomena [22].

3.1.3. *Different stages of recrystallization*

After cold rolling, metals will present changes in their mechanical properties such as increase in hardness and mechanical strength and ductility loss. However, these properties can be partially restored upon annealing. The first stage of annealing is the recovery, where dislocations are rearranged to reduce the energy related to the plastic deformation fields produced by the already existent dislocations and also by the new ones which were generated during deformation. This rearrangement occurs via dislocation annihilation and polygonization. When it happens simultaneously as plastic deformation, it is called dynamic recovery [17,18].

Metals with elevated stacking-fault energy, upon cold work, present complex dislocation structures (cell structure). The development of cellular substructure reduces the interior energy by the reorganization of dislocations in the cell walls. During recovery the energy can still be reduced by reorganization of dislocations in the cell walls, transforming the cell into a sub-grain. These sub-grains can rotate and coalesce to reduce even more the energy of the system [17]. It is therefore difficult to determine the beginning and the end of the recovery phenomenon. On the other hand, the recrystallization is easier to observe, once it involves the formation and growth of new strain-free grains which are formed by nucleation and growth [18].

Nucleation occurs, preferentially, at high energy sites such as high-angle grain boundaries (HAGBs), precipitate interfaces and in the structures generated due to deformation heterogeneities.

Figs. 6 and 7 show IPF maps and ODFs of the steel 430Nb while Figs. 8 and 9 display IPF maps and ODFs of the steel ASTM 439 at different stages of recrystallization with interrupted annealing at temperatures T1 (700 °C), T2 (770 °C), T3 (800 °C) and T4 (830 °C).

During the annealing of the 430Nb steel, samples T1 and T2 still display a highly deformed microstructure with strong texture, see Fig. 6(a) and (b). According to the ODFs, Fig. 7(a) and (b), the changes in the texture were restricted to α and γ fibers and rotated cube component. In both conditions, the peak appeared close to the α-fiber component (223) [1$\bar{1}$0]. In T1 condition a second maximum is present close to the γ-fiber component (111) [0$\bar{1}$1], whereas, in T2 condition, the second maximum is close to the rotated cube component.

In the IPF maps of the conditions T3 and T4, Fig. 6(c) and (d), it is already possible to notice new grains in the deformed matrix. These grains were responsible for changing the texture and reducing its maximum intensity. Fig. 7(c) and (d) show peaks close to the ideal components (114) $\left[1\bar{1}0\right]$ and (112) $\left[1\bar{1}0\right]$ of the conditions T3 and T4, respectively.

Fig. 8 displays a similar behavior for the ASTM 439 steel as for 430Nb. Conditions T1 and T2 presented highly deformed matrix and strong texture components, as can be seen in Fig. 8(a) and (b). The ODF shows a peak close to (223) [1$\bar{1}$0] (10.1 times random) and a second maximum at the γ-fiber component (111) [0$\bar{1}$1] for condition T1, Fig. 9(a), whereas Fig. 9(b) presents a peak close to the rotated cube component (001) [1$\bar{1}$0] for condition T2.

In Fig. 8(c) and (d), it is possible to notice the beginning of recrystallization through the formation of new grains in the IPF maps at temperatures T3 and T4. These grains are smaller than the ones observed in the same conditions in the steel 430Nb. ODFs of the Fig. 9(c) and (d) show peaks close to the α-fiber component (112) [1$\bar{1}$0] (10 times random) for both conditions and a weak γ-fiber texture.

The larger grains at condition T3 in steel 430Nb lead to the observation that recrystallization occurs faster in comparison with steel ASTM 439. This observation, here revealed by EBSD analysis, supports our previous work [15] where this fact was pointed out by optical microscopy and Vickers micro-hardness test and was discussed in detail. This behavior can be ascribed to the higher amount of carbon and nitrogen, which can create more precipitates that acts as sites for heterogeneous nucleation, and the lower annealing temperature, which increases the driving force for precipitates formation.

During recrystallization of both steels, changes were observed in rotated cube components and in the α and γ fibers. The α-fiber orientations between {001}<110> and {112}<110> are believed to have lower stored energy in comparison with

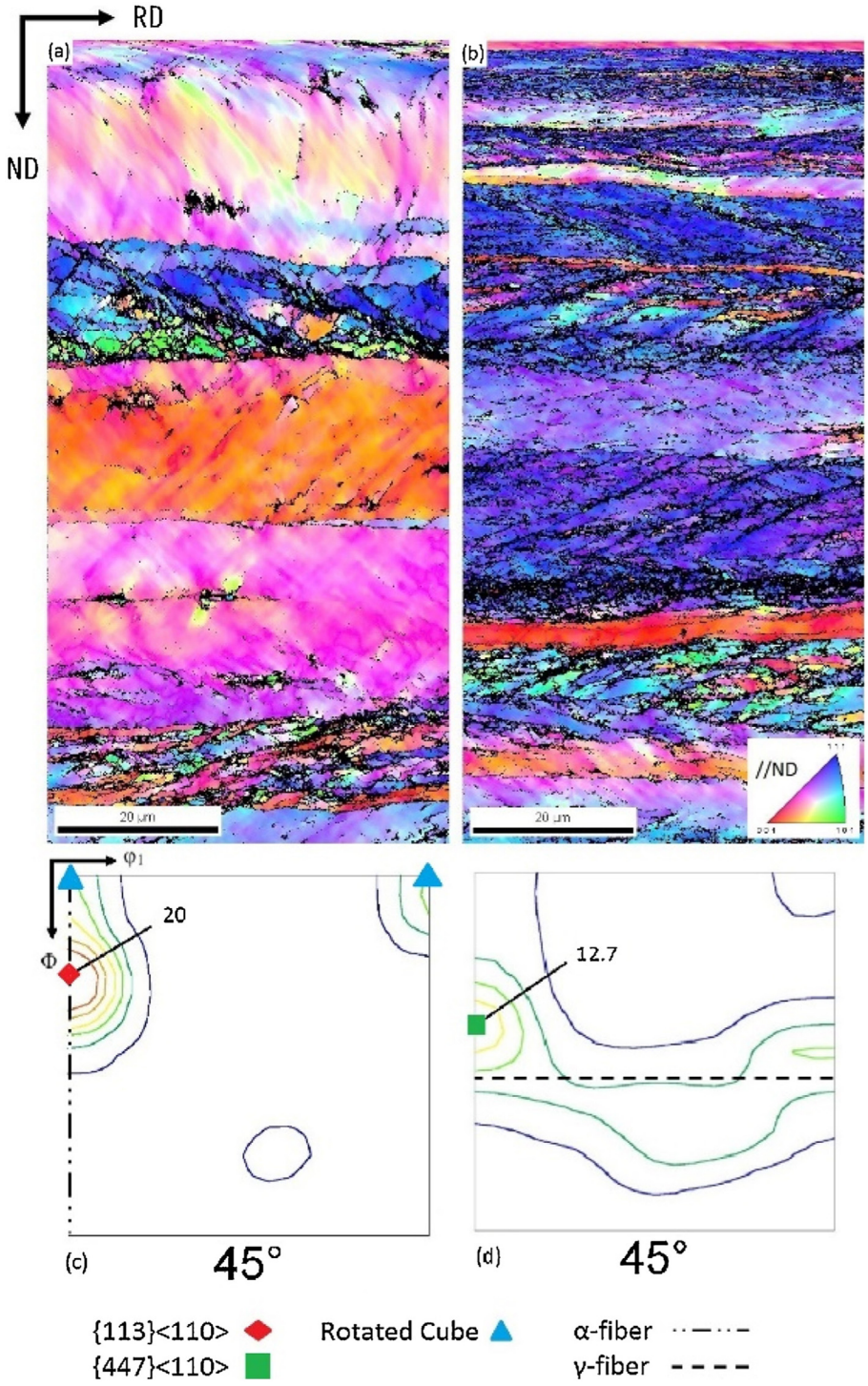

Fig. 5 – Cold rolled condition: (a) and (b) IPF maps and (c) and (d) ODF sections of the steels 430Nb and ASTM 439, respectively. Color code parallel to ND. $\varphi_2 = 45°$, Φ and φ_1 range from 0 to 90°. Texture levels: 1-5-7-10-13-20.

γ-fiber. In this way, new grains will tend to nucleate, preferentially, in grains with γ-fiber orientation, thus, growing at expense of other orientations including the α-fiber [23].

3.1.4. *Recrystallized samples*

Fig. 10 shows the IPF maps and ODFs of the annealed condition for both materials.

As can be seen in Fig. 10(a) and (b), the annealing produced a fully recrystallized microstructure with a predominance of γ-fiber, blue color ({111}//ND). Fig. 10(c) and (d) show, for both conditions, a peak in the component (554) [$\bar{2}\bar{2}5$] (shifted $\bar{5}°\Phi$ from {111}<112>) and a second maximum at (111) [$1\bar{2}1$]. These two components were more pronounced in ASTM 439 steel. As pointed out by Verbeken et al. [24], severe rolling can cause

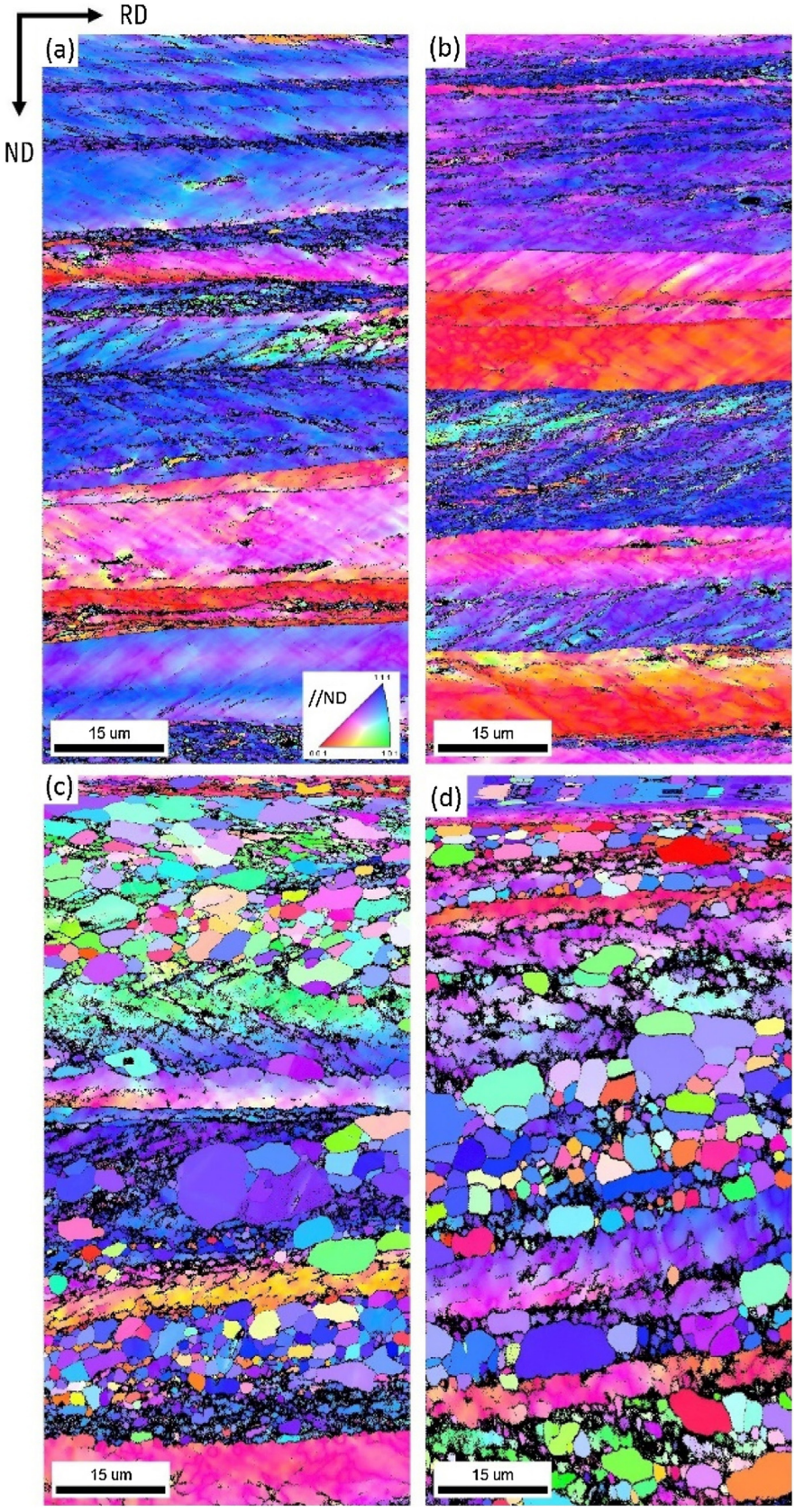

Fig. 6 – IPF maps of the steel 430Nb at different stages of annealing (a) temperature T1, (b) temperature T2, (c) temperature T3 and (d) temperature T4. Color code parallel to ND.

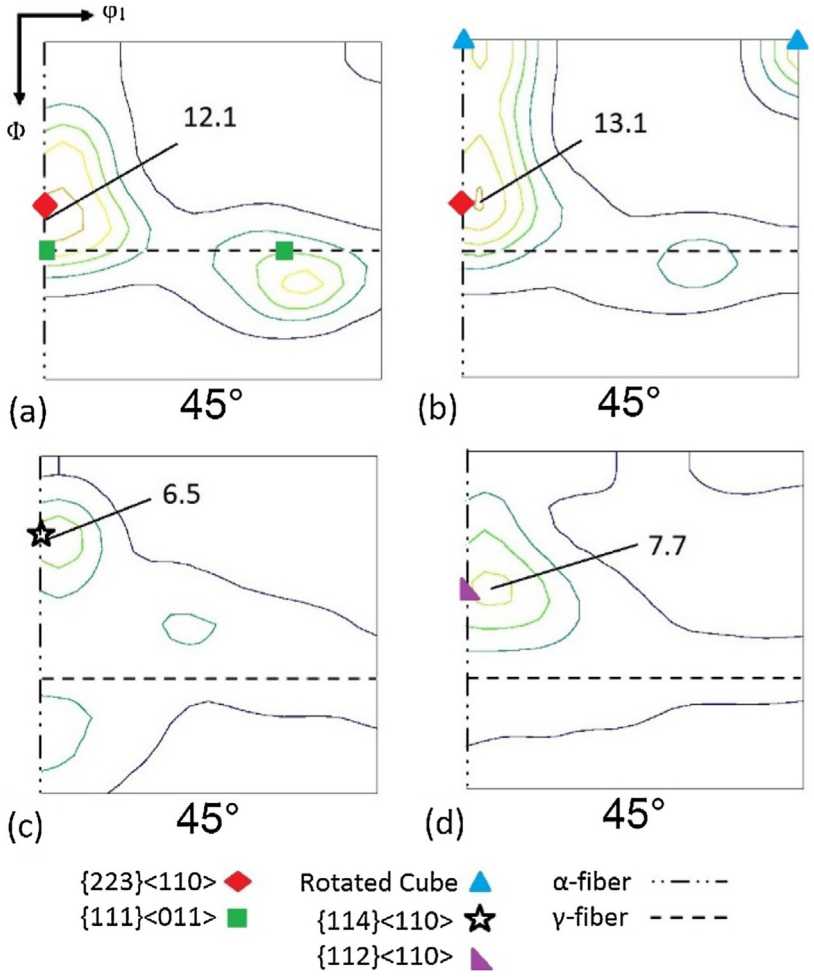

Fig. 7 – ODFs of the steel 430Nb at different stages of annealing (a) temperature T1, (b) temperature T2, (c) temperature T3 and (d) temperature T4. $\varphi_2 = 45°$, Φ and φ_1 range from 0 to 90°. Levels: 1-3-5-7-10-13.

specific components, {554}<225> and {113}<471>, to appear during the final stages of recrystallization in ultra-low carbon steels.

The preferential crystallographic orientation that may develop upon annealing is ascribed to two different mechanisms that can act at once and/or prevail at different stages of recrystallization: oriented nucleation and selective growth [17]. On the one hand, oriented nucleation assumes that grains with a specific orientation nucleate first and therefore dominate the final texture after complete recrystallization. Therefore these orientations will have a size advantage, in comparison with other orientations, that will prevail until the end of the annealing determining the texture after final recrystallization. On the other hand, selective growth involves the rapid increase in size of nuclei with specific misorientation with respect to the matrix, which means that the first nuclei will not determine the final texture and texture gradually changes due to the fact that specific grain boundaries display increased mobility compared to others [25].

The recrystallization textures of heavily deformed low carbon steels sheets show features related to both mechanisms: preferred nucleation at high-angle grain boundaries (HAGBs) between the deformed grains and selective growth during the later stages of recrystallization [24–26]. Because of the deformation gradient along the thickness of the sheet and the role played by both aforementioned mechanisms, the annealed texture significantly differed from the cold rolled texture.

After recrystallization, the intensity of the {111}<112> component increased whereas the {111}<110> component was reduced. Some studies [26–28] have argued that due to local strain gradients that persist in the vicinity of the grain boundaries, the new grains formed are subjected to rotations about the normal direction with respect to the matrix, which means that regions located between two symmetrically equivalent components {111}<110> may actually comprise the {111}<112> component. Therefore, in the presence of the dominant cold rolled {111}<110> texture component, {111}<112> will nucleate and, eventually, prevail in the final annealed texture. However, the maximum texture components are located close to {334}<4$\bar{8}$3> which is deviated about 8° from the ideal {111}<112> [29]. Raabe and Lücke [20] have proposed that this component may develop from preferred growth in the {112}<110> deformation component in FSS. The present work also supports the predominance of the {334}<4$\bar{8}$3> component in annealed FSS. This behavior is observed in the ODFs presented in Fig. 10(c) and (d).

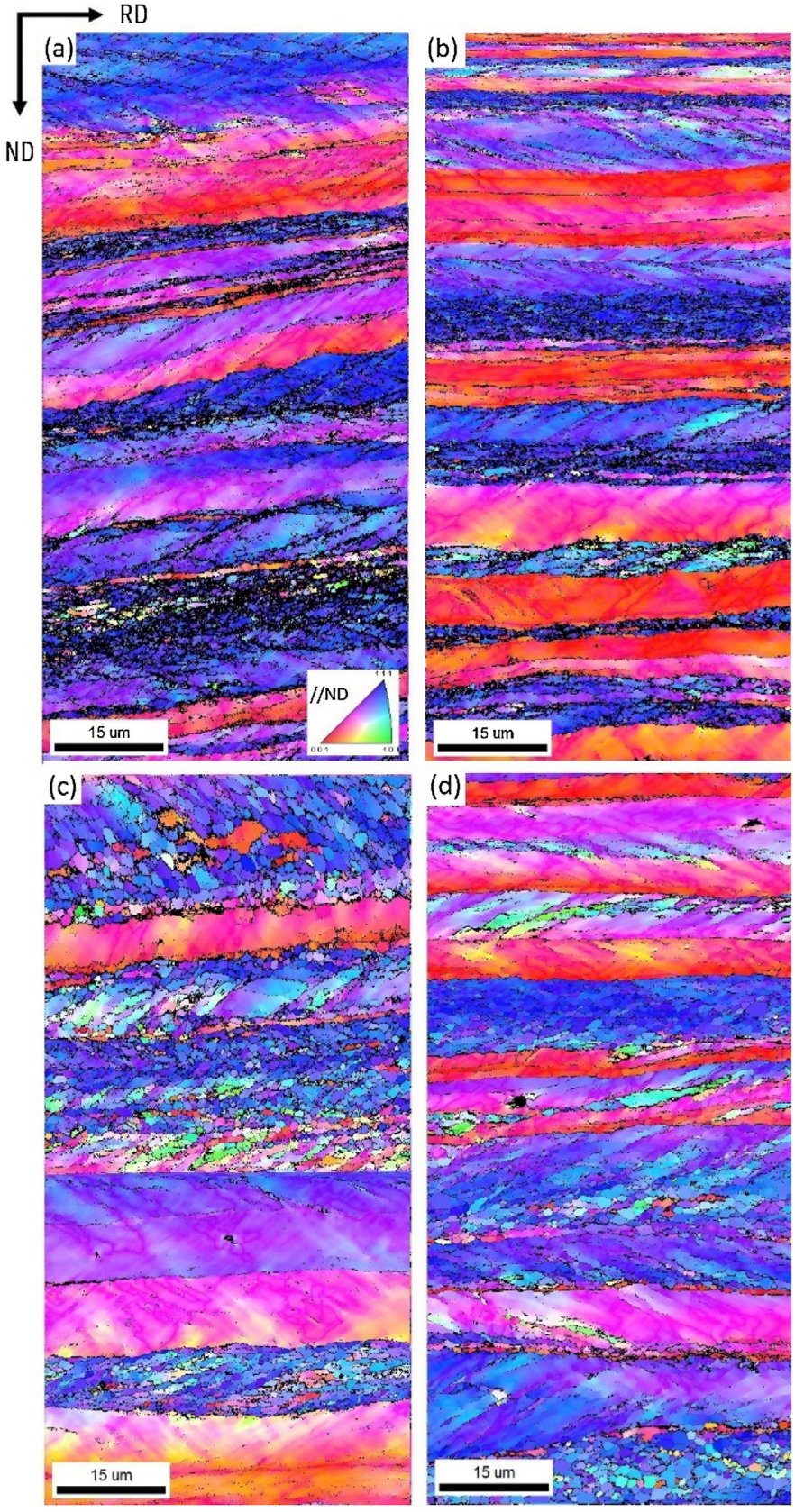

Fig. 8 – IPF maps of the steel ASTM 439 at different stages of annealing (a) temperature T1, (b) temperature T2, (c) temperature T3 and (d) temperature T4. Color code parallel to ND.

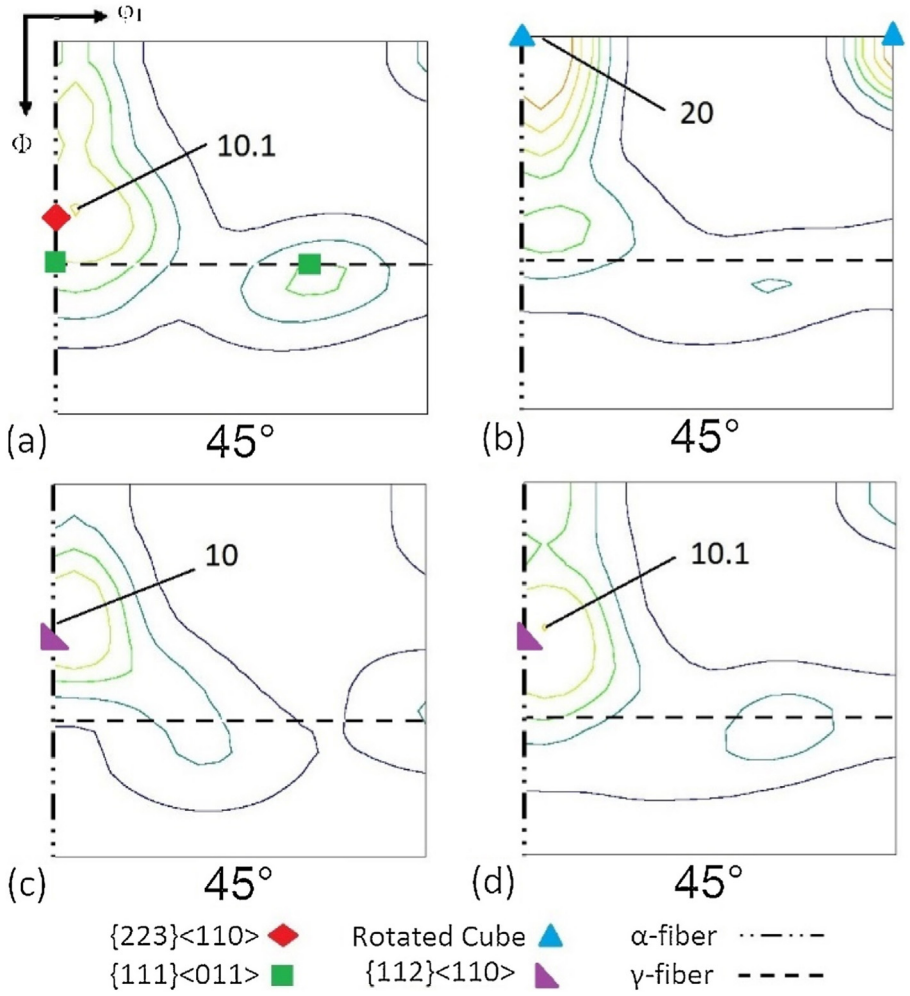

Fig. 9 – ODFs of the steel ASTM 439 at different stages of annealing (a) temperature T1, (b) temperature T2, (c) temperature T3 and (d) temperature T4. $\varphi_2 = 45°$, Φ and φ_1 range from 0 to 90°. Levels: 1-3-5-7-10-13.

The average grain size values are 16 and 19 μm for 430Nb and ASTM 439, respectively. Smaller grains of 430Nb steel can be linked to weak texture components and are related to three different factors that were discussed in previous works [7,15]: the higher volume fraction of precipitates, the higher amount of carbon and nitrogen in solid solution and the lower annealing temperature. The smaller the grains, the higher the number of grains and also the probability of obtaining a weaker texture upon annealing.

According to Takahashi and Okamoto [30], the addition of C or N results in the weakening of γ-fiber recrystallization texture, once the interstitial atoms affect the annihilation and the migration of dislocations during recovery and the nucleation stages of recrystallization. Interstitial atoms can also migrate to grain boundaries hindering their mobility, which contributes to smaller final grain sizes and, therefore, weaker texture, as can be seen in 430Nb steel.

A closer look at the Fig. 11 allows a better understanding of the evolution of α and γ fibers texture intensity during annealing.

Analyzing the α-fiber, Fig. 11(a) and (c), one can notice that, for both steels, the conditions as-received (AR) and annealed (A) display similar behavior: low intensities (between 1 and 4) and homogeneous distribution. In the intermediate conditions, starting from the cold rolled (CR) samples, there is a trend toward intensity reduction and a shift of the peaks towards $\Phi = 55°$ (this is the location of a component at the intersection of the α and γ fibers, (111)[$1\bar{1}0$]). As the annealing is carried out, α-fiber became more homogeneous and less pronounced.

Regarding γ-fiber, in AR and CR conditions the intensities are low (between 0 and 2 for 430Nb and between 2 and 4 for ASTM 439) and the intensity distributions are homogeneous. As the annealing is taking place, the intensities tend to increase and the peaks change from the position {111}<110>, both $\varphi_1 = 0°$ and $\varphi_1 = 60°$, to {111}<112>, $\varphi_1 = 30°$ and $\varphi_1 = 90°$. This distribution is more homogeneous in 430Nb steel (ranges from 4 to 6, against 4 to 10 in ASTM 439) in the annealed condition. The analysis of Fig. 11 clarifies the results shown in the ODFs and is in accordance with the observation of smaller grains at the end of the recrystallization.

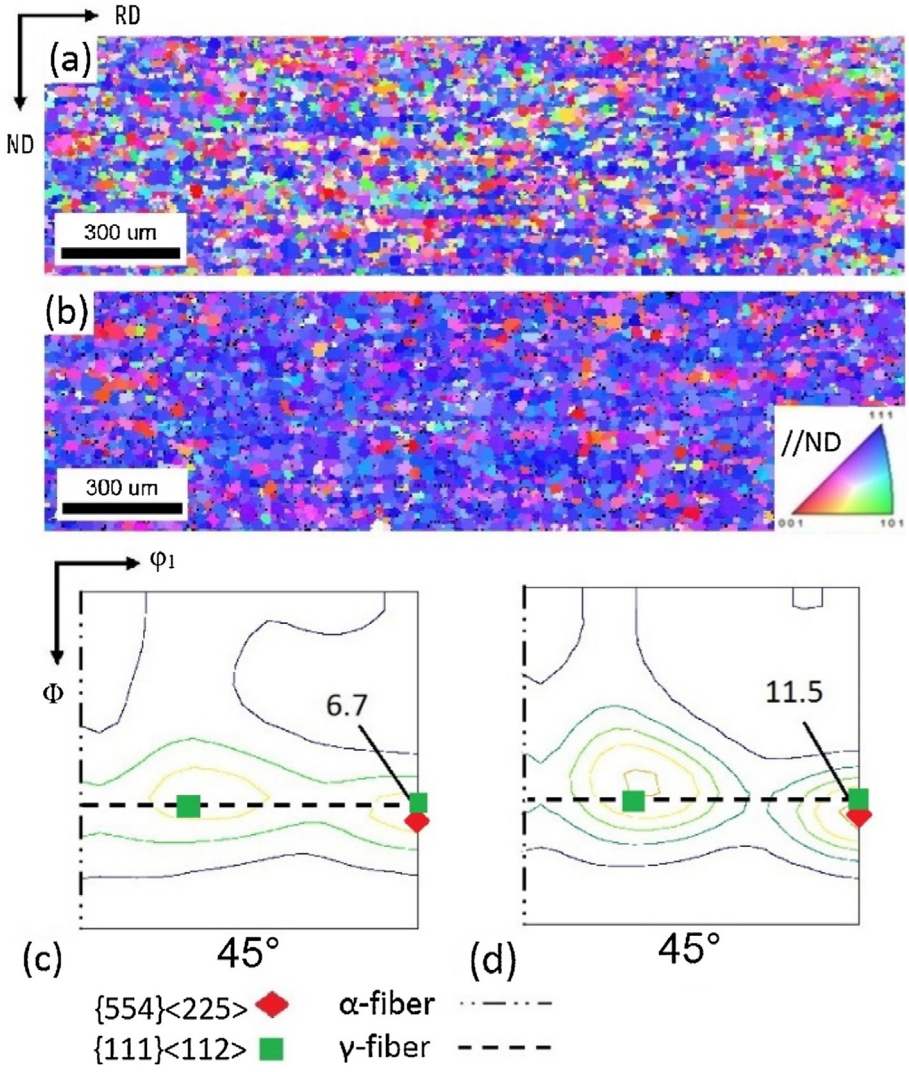

Fig. 10 – (a) and (b) IPF maps, (c) and (d) ODFs of the steel 430Nb and ASTM 439, respectively, in the annealed condition. (a) and (b) color code parallel to ND. (c) and (d) $\varphi_2 = 45°$, Φ and φ_1 range from 0 to 90°. Levels: 1-3-5-7-10-13.

3.2. *Grain boundaries*

The grain boundary character distributions (GBCD) of the 430Nb and ASTM 439 steels for all analyzed conditions are summarized in Fig. 12(a) and (b), respectively. The differences in the as-received conditions, hot rolling followed by annealing for 430Nb and only hot rolling for ASTM 439 are clear. The majority of the grain boundaries for the 430Nb steel are HAGBs, i.e. misorientation angles >15°, whereas the low angle grain boundaries (LAGBs), i.e. misorientation angles between 2 and 15°, are predominant for ASTM 439.

For the analysis of Coincidence Site lattices (CSL) boundaries, the boundary fraction (Σ3–Σ29) was determined following the Brandon's criterion allowing a maximum permissible deviation given by an equation of the form $\Delta\theta = \theta_0(\Sigma)^{-n}$ where $\theta = 15$ and $n = 0.5$ [31]. These special boundaries can play an important role in intergranular corrosion resistance and crack propagation [32,33].

After cold rolling, as expected for both steels, the microstructures are dominated by LAGBs, because of the formation of sub-grains during cold work. The presence of HAGBs is due to accumulation of dislocations [5]. Significant changes appear upon annealing, where the rearrangement of dislocations, recovery and recrystallization phenomena are responsible for the fraction increase of HAGBs at expense of LAGBs [17].

With respect to CSL boundaries, there is an increase as the annealing is carried out with some variations at different stages of recrystallization as can be seen in the CSL boundaries distributions in Fig. 13.

The most prominent CSL boundaries for both materials are Σ3 and Σ13b. Σ3 is a low energy and low mobility boundary type defined by a rotation of 60° around a common axis <111>. This is the same rotation between the components with significant intensity in the ODF that belong to the same family planes and directions such as (111) [1$\bar{1}$0]/(111) [0$\bar{1}$1] and (111) [1$\bar{2}$1]/(111) [$\bar{1}$12]. Σ3 boundaries could be formed thanks to the grain rotation during cold rolling as an attempt to achieve the lowest energy configuration. This fraction will tend to increase as the annealing is carried out [5,34].

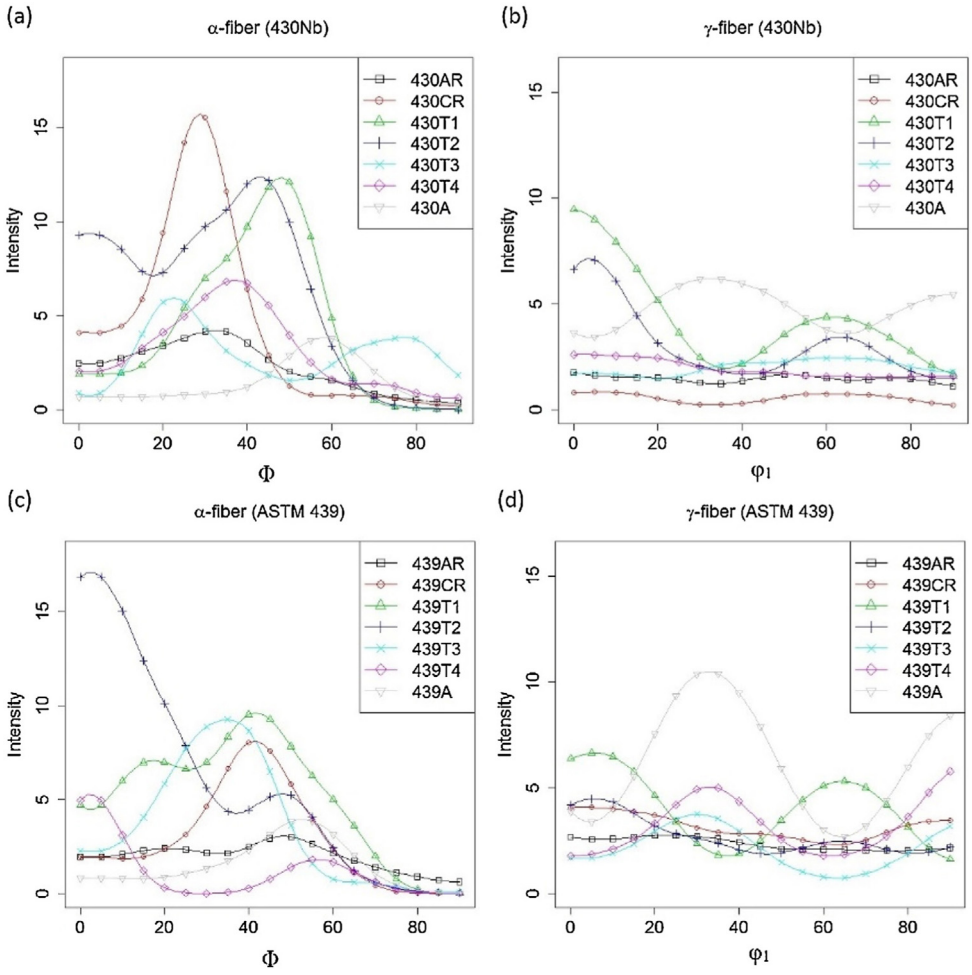

Fig. 11 – (a) and (c) α and (b) and (d) γ fibers evolution of the steels 430Nb and ASTM 439, respectively.

Σ13b is a high mobility boundary [17] defined by the rotation of 27.8° around <111> which is very close to the misorientation between the two family planes aforementioned {111}<110> and {111}<112>, 30° around <111>, which are the most important components of the γ-fiber. Besides the peaks at Σ3 and Σ13b for condition T3 of 430Nb steel, both materials displayed a similar CSL boundaries distributions. To investigate and clarify the effect of Ti addition on ASTM 439 CSL boundaries, an in-depth study on recrystallization kinetics with more intermediate annealing temperatures must be done.

3.3. *Precipitate characterization*

Fig. 14(a)–(c) show the two types of precipitates found in 430Nb steel: light ones and dark ones. Most of the smaller precipitates (light) are, approximately round and can be seen as white dots on the secondary electrons images and are found either within the grains or at the grain boundaries whereas the dark precipitates are located preferentially at grain boundaries. The larger precipitates appear lying in the rolling direction (horizontal) and seem to be broken due to the cold rolling. They can be as large as 6 μm in their largest dimension.

Analysis of energy dispersive X-ray spectroscopy (EDS) has shown that the dark precipitates (e.g. point 1 in Fig. 14(a)) are inclusions rich in oxygen and silicon and can also present high amounts of magnesium, aluminum and calcium (elements, most likely, originated from the steelmaking industrial process). On the other hand, the light precipitates (e.g. point 2 in Fig. 14(a) and points 1 and 2 in Fig. 14(b) are rich in niobium and can be as large as 4 μm.

Fig. 14(d)–(f) show precipitates of ASTM 439 steel. Fig. 14(d) represents a peculiar precipitate within the Ti-stabilized steels: the center (point 1) is composed by titanium and nitrogen in a dark and round shape, which can be as large as 2 μm, surrounded by a polygonal precipitate (point 2) also rich in titanium and nitrogen but with small amounts of Nb, C and O. These are the same components as those present in the dark regions (points 3 and 4 of Fig. 14(d) and point 1 of Fig. 14(e)) whereas the light regions (points 2 and 3 of Fig. 14(e)) are richer in Nb. The size of the polygons ranges from 4 to 8 μm in their largest dimension.

Titanium nitrides are formed at high temperatures (in the liquid phase of steel) and, after solidification, they remain practically unchanged [35]. Niobium will preferentially combine with carbon, instead of titanium, during the cooling of

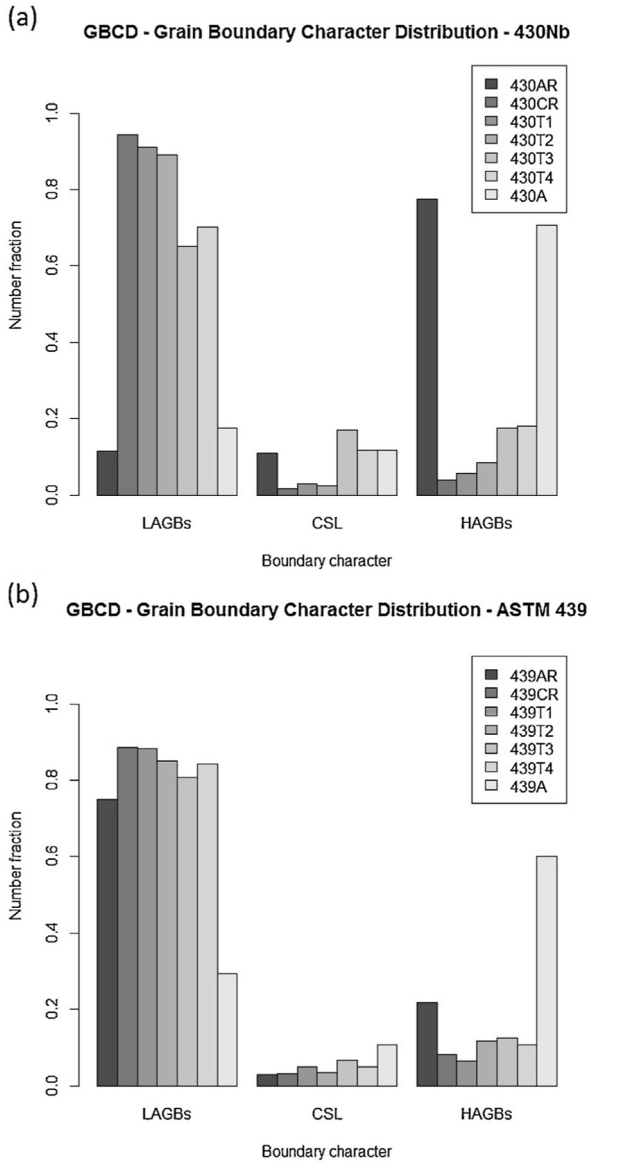

Fig. 12 – Grain Boundary Character Distributions (GBCD) of (a) 430Nb and (b) ASTM 439 in all conditions. AR: as-received, CR: cold rolled, T1: interrupted annealing at 700 °C, T2: interrupted annealing at 770 °C, T3: interrupted annealing at 800 °C, T4: interrupted annealing at 830 °C and A: annealed.

liquid steel [5]. The interface of these primary precipitates will act as preferential sites for heterogeneous nucleation of Ti carbonitrides and Nb carbonitrides being responsible for the peculiar shape of these coarse precipitates in ASTM 439. Cavazos had already observed similar precipitates in a study of FSS stabilized with Zr and Ti [6].

Fig. 14(c) and (f) are representative images for the specific alloys and therefore allow a qualitative comparison of the volume fraction and distribution of precipitates in both steels. The larger amount of precipitates is responsible for the smaller grain size and the weaker γ-fiber texture in 430Nb, because they stimulated the nucleation of new grains through the particle stimulated nucleation (PSN) mechanism [17]. Furthermore, the amount of Nb and Ti in solid solution plays an important role since both tend to migrate to grain boundaries decreasing both nucleation and growth rates [18]. The amount of Nb (weight %) in solid solution for mono-stabilized steels (430Nb) is given by $\Delta Nb = \%Nb - 6.6\%N - 7.74\%C$ while the amounts of Nb and Ti in bi-stabilized steels (ASTM 439) are given by $\Delta Nb = \%Nb - 5.42\%C$ and $\Delta Ti = \%Ti - 1.2\%C - 3.42\%N$, respectively [36]. The resulting values of ΔNb are 0.037% and 0.136% in 430Nb and ASTM 439 steels, respectively, while the ΔTi value is 0.100% for ASTM 439 steel. Apart from the lower level of atoms in solid solution in the 430Nb, the lower annealing temperature resulted in a larger undercooling that promoted the formation of a fine and dense precipitate distribution. Both factors gave rise to the faster recrystallization of 430Nb and as such confirmed the EBSD analysis. Gao et al. [14] have also demonstrated that a fine and dense distribution of precipitates promote the formation of some heterogeneities in the microstructure during cold rolling (as previously discussed in this paper). Recrystallization nuclei that may form on these heterogeneities are prone to have a random crystallographic orientation, therefore, weakening the γ-fiber.

Table 1 – Mechanical properties of the steels 430Nb and ASTM 439.

Tensile properties	430Nb	ASTM 439
$YS_{(0°)}$ [MPa]	291 ± 4	281 ± 3
$YS_{(45°)}$ [MPa]	310 ± 8	288 ± 1
$YS_{(90°)}$ [MPa]	296 ± 7	295 ± 2
YS [MPa]	291 ± 4	281 ± 3
UTS [MPa]	460 ± 3	465 ± 2
Uniform Elongation [%]	22.4 ± 0.3	22.8 ± 0.2
Drawability		
R_0	1.45 ± 0.01	1.86 ± 0.02
R_{45}	1.09 ± 0.04	1.73 ± 0.11
R_{90}	1.36 ± 0.18	2.15 ± 0.05
$\bar{R}$	1.25 ± 0.03	1.87 ± 0.05
ΔR	0.31 ± 0.13	0.28 ± 0.14
LDR	2.18	>2.30

3.4. *Mechanical properties*

Mechanical properties were determined by tensile test and Swift test. The results are summarized in Table 1 as yield stress (YS), ultimate tensile strength (UTS) and uniform elongation. The YS was also evaluated for samples taken along three different angles with respect to the rolling direction: 0, 45 and 90°. The average normal anisotropy coefficient value, $\bar{R}$, and the planar anisotropy coefficient, ΔR, were calculated and are shown together with the limit drawing ratio, LDR, for both steels, in Table 1.

Steel 430Nb presented slightly higher values for YS in comparison with ASTM 439. The UTS and the uniform elongation were considered equal as differences are within the experimental error. The addition of stabilizing elements such as niobium in 430Nb steel and titanium and niobium in ASTM 439 affect the microstructure and can promote an increase in the yield stress via three different mechanisms: precipitation, grain refinement and solid solution [18,35].

The higher values for $\bar{R}$ and LDR for the ASTM 439 steel are in accordance with the stronger γ-fiber developed upon

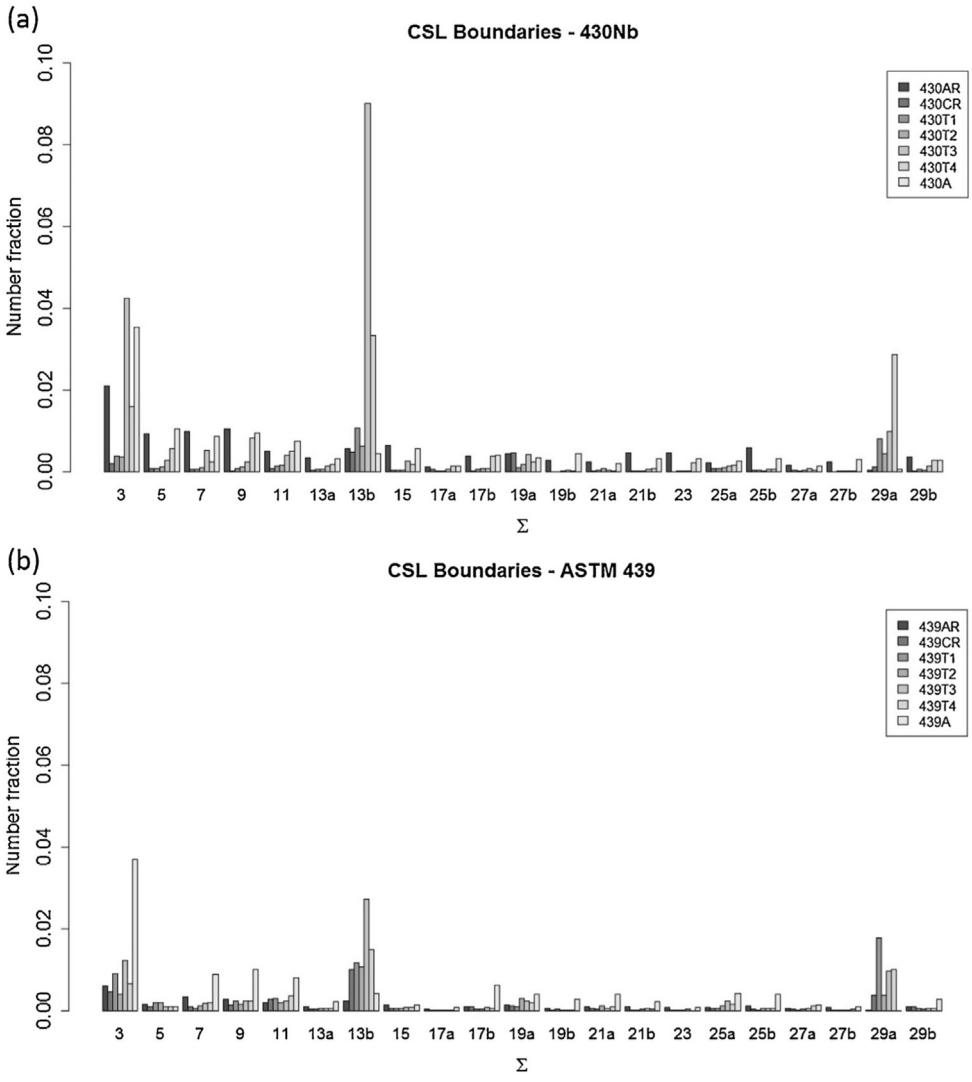

Fig. 13 – Coincidence Site Lattices (CSL) Boundaries distributions of the steels (a) 430Nb and (b) ASTM 439. AR: as-received, CR: cold rolled, T1: interrupted annealing at 700 °C, T2: interrupted annealing at 770 °C, T3: interrupted annealing at 800 °C, T4: interrupted annealing at 830 °C and A: annealed.

annealing. These results mean that it is possible to produce deeper blankets with this steel, since it is more resistant to thinning. With respect to the LDR specimens, the 430Nb steel developed four ears at 0 and 90° with respect the rolling direction. The position of the ears is in accordance with the values of YS, as $YS_{(45°)}$ was slightly larger than $YS_{(0°)}$ and $YS_{(90°)}$ (positions susceptible to ear formation). On the other hand, ASTM 439 developed six ears located at 0, 60 and 120°. These positions are also in accordance with $YS_{(90°)} > YS_{(45°)} > YS_{(0°)}$. At 0° the material is prone to ear formation (lowest $YS_{(0°)}$) and at 90° it is difficult to develop ears (largest $YS_{(90°)}$) because it is the least probable location (30° away from the closest ear location).

The six-ear profile is linked to the main γ-fiber components, {111}<112> and {111}<110>, and can be explained in terms of the corresponding symmetry of the Schmid tensors of the {111}<uvw> texture components. This behavior is shown in detail in a study conducted by Raabe et al. [37] where the number of ears developed during cup drawing of low carbon steels was investigated. The four-ear profile, on the other hand is related to a strong presence of the rotated cube component ($\varphi_1 = 0°$, $\Phi = 0°$ and $\varphi_2 = 45°$) and results in four large ears. The severity of the ears, i.e. their height, can be assessed by ΔR and was equal for both steels considering the average experimental error as indicated in Table 1.

The less pronounced γ-fiber on the 430Nb steel could have caused the smaller number of ears. Similar behavior was observed by Davison [38] when comparing texture and planar anisotropy of cold rolled and annealed sheets of a Nb-stabilized and a Ti-stabilized 18%Cr 2%Mo FSSs. When Ti was present, six distinct ears could be observed at 0, 60 and 120° to the rolling direction, whereas for the Nb-stabilized sheets it was difficult to precisely determine the number of ears. The ear along the rolling direction was very small but distinct while the other ears were not clearly defined. In Davison [38] study, the sheets underwent 85% of thickness reduction in one and/or two cold rolling steps leaving a considerable {001}<110> texture component in the materials (even after annealing) affecting the occurrence of earing.

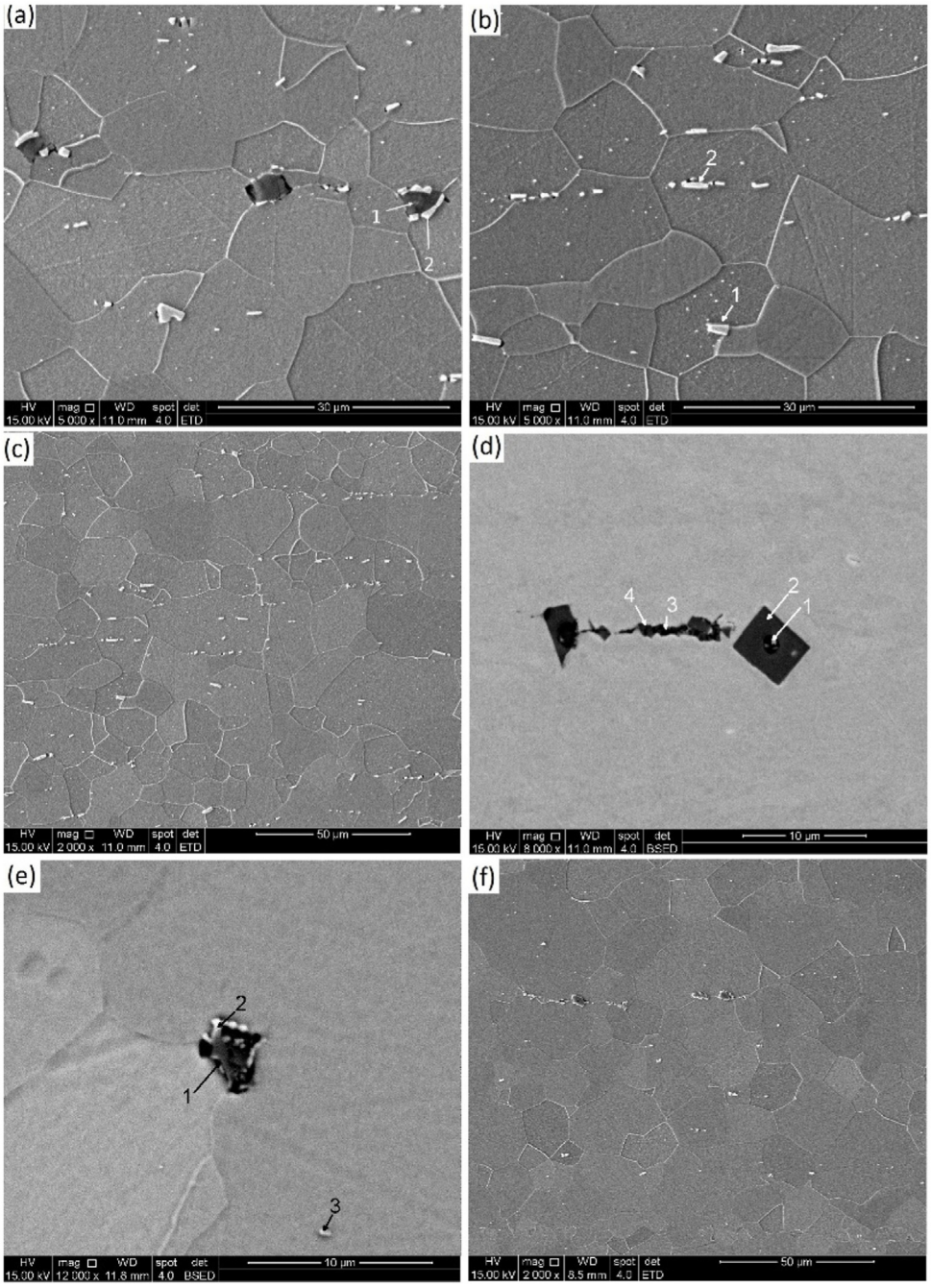

Fig. 14 – Scanning electron micrographs of precipitates in both materials: (a), (b) and (c) for steel 430Nb and (d), (e) and (f) for steel ASTM 439.

In the present paper, the annealed condition of both steels, 430Nb and ASTM 439, exhibited intense γ-fiber components, primarily {111}<112>, without rotated cube component. Therefore, the earing behavior can be ascribed to the distribution of the γ-fiber. The heterogeneous distribution showed by the ASTM 439 steel (with intensities ranging from 4 to 10 times random according to Fig. 11d), leaded to six-ear formation while a less heterogeneous distribution, as can be seen in 430Nb (texture intensities ranging from 4 to 6 times random, see Fig. 11b), resulted in four ears. The occurrence of the two major components of γ-fiber, {111}<112> and {111}<110>, in equal volume fraction would lead to a perfect isotropic shape, i.e. the more homogeneous the γ-fiber distribution is, the better [37].

4. Conclusions

A comparison between the niobium-stabilized ferritic stainless steel type ASTM 430, 430Nb, and niobium-titanium-stabilized ferritic stainless steel ASTM 439 was carried out during different stages of recrystallization. Microstructure,

texture and grain boundary character distribution and their evolution was investigated. The annealed samples were subjected to tensile test and Swift test for evaluation of mechanical performance and deep drawability.

The faster recrystallization on the 430Nb steel, when compared to the ASTM 439, could be ascribed to the following aspects: the larger amounts of C and N in the chemical composition, the lower amount of atoms in solid solution and the lower annealing temperature. All of these factors promoted the formation of a fine and dense distribution of precipitates resulting in a faster recrystallization.

Both materials presented textural variation, essentially, in α and γ fibers as well as rotated cube component. During annealing, γ-fiber is produced at the expense of the α-fiber with intense components close to {111}<112> which were related to the presence of the Coincidence Site Lattice boundary Σ13b. The steel 430Nb presented less pronounced γ-fiber texture due to the larger volume fraction of small precipitates that led to formation of more randomly oriented grains with smaller recrystallized grain size and higher yield stress as a result.

Precipitates in ASTM 439 presented a peculiar shape: small round centers rich in titanium and nitrogen, surrounded by a polygonal structure rich in titanium, nitrogen, carbon, oxygen and niobium. The ASTM 439 steel developed a stronger and more heterogeneous γ-fiber distribution that resulted in better drawability behavior through larger values of average normal anisotropy coefficient, $\bar{R}$, and limit drawing ratio, LDR.

The homogeneity of the γ-fiber distribution was reflected in the number of ears developed during the Swift test. The 430Nb steel exhibited a more homogeneous γ-fiber distribution resulting in a four-ear profile while the ASTM 439 displayed a six-ear profile which concurred with almost twice the intensity of the {111}<112> texture component.

Conflicts of interest

The authors declare no conflicts of interest.

Acknowledgements

The authors would like to acknowledge CAPES, CNPq, FAPEMIG and PROEX/UFMG for financial supportand the Center of Microscopy at the Universidade Federal de Minas Gerais (http://www.microscopia.ufmg.br) and *Aperam South America* for technical support.

REFERENCES

[1] International Stainless Steel Forum - ISSF. In: The Ferritic Solution: Properties; Advantages and Applications; 2007. p. 67.
[2] Lo KH, Shek CH, Lai JKL. Recent developments in stainless steels. Mater Sci Eng R Rep 2009;65:39–104, http://dx.doi.org/10.1016/j.mser.2009.03.001.
[3] You Xiang-mi, Jiang Zhou-hua, Hua-bing LI. Ultra-pure ferritic stainless steel – grade, refining operation, and applications. Iron Steel 2007;14:24.
[4] Krauss G. Steels: processing, structure and performance; 2005.
[5] Yan H, Bi H, Li X, Xu Z. Microstructure and texture of Nb + Ti stabilized ferritic stainless steel. Mater Charact 2008;59:1741–6, http://dx.doi.org/10.1016/j.matchar.2008.03.018.
[6] Cavazos JL. Characterization of precipitates formed in a ferritic stainless steel stabilized with Zr and Ti additions. Mater Charact 2006;56:96–101, http://dx.doi.org/10.1016/j.matchar.2005.05.006.
[7] LP de AR Tanure, de Alcântara CM, de Oliveira TR, Santos DB, Gonzalez BM. Comparison of microstructure and mechanical behavior of the ferritic stainless steels ASTM 430 stabilized with niobium and ASTM 439 stabilized with niobium and titanium. Mater Sci Forum 2016;879:1651–5, http://dx.doi.org/10.4028/www.scientific.net/MSF.879.1651.
[8] Du W, Jiang Lzhu, Sun Qshe, Liu Zyu, Zhang X. Microstructure, texture, and formability of Nb+Ti stabilized high purity ferritic stainless steel. J Iron Steel Res Int 2010;17:47–52, http://dx.doi.org/10.1016/S1006-706X(10)60113-6.
[9] Lee KM, Huh MY, Park S, Engler O. Effect of texture components on the lankford parameters in ferritic stainless steel sheets. ISIJ Int 2012;52:522–9, http://dx.doi.org/10.2355/isijinternational.52.522.
[10] Huh MY, Engler O. Effect of intermediate annealing on texture, formability and ridging of 17%Cr ferritic stainless steel sheet. Mater Sci Eng A 2001;308:74–87, http://dx.doi.org/10.1016/S0921-5093(00)01995-X.
[11] Rodrigues DG, de Alcântara CM, Santos DB, de Oliveira TR, Gonzalez BM. Effects of annealing conditions on recrystallization, texture, and average normal anisotropy coefficient of a niobium-stabilized ferritic stainless steel. Steel Res Int 2017;87:0–12, http://dx.doi.org/10.1002/srin.201700214.
[12] Rodrigues DG, Alcântara CM, Oliveira TR de, Gonzalez BM. Evaluation of intermediate annealing on Nb-Stabilized ferritic stainless steel. Mater Res 2017:1–6, http://dx.doi.org/10.1590/1980-5373-mr-2016-0999.
[13] Costa RJG, Rodrigues DG, Alves HJB, Oliveira TRde, Gonzalez BM. Comparative study of microstructure, texture, and formability between 11CrTi and 11CrTi+Nb ASTM 409 ferritic stainless steel. Mater Res 2017;20:1593–9, http://dx.doi.org/10.1590/1980-5373-mr-2017-0173.
[14] Gao F, Liu ZY, Wang GD. Effect of the size and dispersion of precipitates formed in hot rolling on recrystallization texture in ferritic stainless steels. J Mater Sci 2013;48:2404–15, http://dx.doi.org/10.1007/s10853-012-7027-5.
[15] Tanure LP de AR, Alcântara CM, Oliveira TR de, Santos DB, Gonzalez BM. Microstructure, texture and microhardness evolution during annealing heat treatment and mechanical behavior of the niobium-stabilized ferritic stainless steel ASTM 430 and niobium-titanium-stabilized ferritic stainless steel ASTM 439: a comparative study. Mater Res 2017;20:1650–7, http://dx.doi.org/10.1590/1980-5373-mr-2017-0568.
[16] Rodrigues DG, Oliveira TR de, Santos DB, Gonzalez BM. Influence of annealing heating rate on Nb ferritic stainless steel microstructure and texture. Mater Sci Forum 2013;753:217–20, http://dx.doi.org/10.4028/www.scientific.net/MSF.753.217.
[17] Humphreys FJ, Hatherly M. Recrystallization and related annealing phenomena. 3rd ed; 2004, http://dx.doi.org/10.1016/B978-0-08-044164-1.X5000-2.
[18] Abbaschian R, Abbaschian L, Reed-Hill RE. Physical metallurgy principles. 4th ed. Stamford: CENGAGE Learning; 2009.
[19] Umemoto M, Guo ZH, Tamura I. Effect of cooling rate on grain size of ferrite in a carbon steel. Mater Sci Technol 1987;3:249–55.

[20] Raabe D, Lücke K. Textures of ferritic stainless steels. Mater Sci Technol 1993;9:302–12, http://dx.doi.org/10.1179/026708393790172132.
[21] Han J, Li H, Barbaro F, Zhu Z, Jiang L, Xu H, et al. Effects of processing optimisation on microstructure, texture, grain boundary and mechanical properties of Fe-17Cr ferritic stainless steel thick plates. Mater Sci Eng A 2014;616:20–8, http://dx.doi.org/10.1016/j.msea.2014.07.107.
[22] Dieter GE. Mechanical metallurgy. London: SI Metric; 1988.
[23] Samajdar I, Verlinden B, Van Houtte P, Vanderschueren D. Gamma-fibre recrystallization texture in IF-steel: an investigation on the recrystallization mechanisms. Mater Sci Eng A 1997;238:343–50.
[24] Verbeken K, Kestens L, Jonas JJ. Microtextural study of orientation change during nucleation and growth in a cold rolled ULC steel. Scr Mater 2003;48:1457–62, http://dx.doi.org/10.1016/S1359-6462(03)00078-2.
[25] Verbeken K, Kestens L. Nucleation of secondary recrystallization in ultra low carbon steel. Mater Sci Forum 2005;495–497:1189–94, http://dx.doi.org/10.4028/www.scientific.net/MSF.495-497.1189.
[26] Huh M, Engler O. Effect of intermediate annealing on texture, formability and ridging of 17% Cr ferritic stainless steel sheet. xxx 2001;308:74–87.
[27] Tse YY, Liu GL, Duggan BJ. Deformation banding and nucleation of recrystallization in IF steel. Scr Mater 1999;42:25–30, http://dx.doi.org/10.1016/S1359-6462(99)00303-6.
[28] Hutchinson WB. Recrystallisation textures in iron resulting from nucleation at grain boundaries. Acta Metall 1989;37:1047–56, http://dx.doi.org/10.1016/0001-6160(89)90101-6.
[29] Huh M-Y, Lee J-H, Park SH, Engler O, Raabe D. Effect of Through-thickness macro and micro-texture gradients on ridging of 17%Cr ferritic stainless steel sheet. Steel Research Int 2005;76:797–806.
[30] Takahashi M, Okamoto A. Effect of nitrogen on recrystallization kinetics of extra-low-Carbon steel sheet. Tetsu-to-Hagane 1978;64:2167–76.
[31] Brandon DG. The structure of high-angle grain boundaries. Acta Metall 1966;14:1479–84, http://dx.doi.org/10.1002/pssb.19690310123.
[32] Lehockey EM, Palumbo G, Lin P, Brennenstuhl AM. On the relationship between grain boundary character distribution and intergranular corrosion. Scr Mater 1997;36:1211–8, http://dx.doi.org/10.1016/S1359-6462(97)00018-3.
[33] Watanabe T. The importance of Grain Boundary Character Distribution (GBCD) to recrystallization, grain growth and texture. Scr Metall Mater 1992;27:1497–502.
[34] Saha R, Ray RK. Microstructural and textural changes in a severely cold rolled boron-added interstitial-free steel. Scr Mater 2007;57:841–4, http://dx.doi.org/10.1016/j.scriptamat.2007.06.064.
[35] Najafi H, Rassizadehghani J, Halvaaee A. Mechanical properties of as cast microalloyed steels containing V, Nb and Ti. Mater Sci Technol 2007;23:699–705, http://dx.doi.org/10.1179/174328407X179755.
[36] Oliveira TR. Effet du niobium et du titane sur la déformation à chaud d'aciers inoxydables ferritiques stabilisés. l'Université Jean Monnet de Saint-Étienne; 2003.
[37] Raabe D, Wang Y, Roters F. Crystal plasticity simulation study on the influence of texture on earing in steel. Comput Mater Sci 2005;34:221–34, http://dx.doi.org/10.1016/j.commatsci.2004.12.072.
[38] Davison RM. Texture and anisotropy of low-interstitial 18 pct Cr-2 pct Mo ferritic stainless steel. Metall Trans A 1975;6A:2243–8.